

See discussions, stats, and author profiles for this publication at: <https://www.researchgate.net/publication/231240997>

Carbon Scaffolds for Stiff and Highly Conductive Monolithic Oxide–Carbon Nanotube Composites

ARTICLE *in* CHEMISTRY OF MATERIALS · MAY 2011

Impact Factor: 8.35 · DOI: 10.1021/cm200426k

CITATIONS

19

READS

52

8 AUTHORS, INCLUDING:



[Marcus A Worsley](#)

Lawrence Livermore National Laboratory

90 PUBLICATIONS 1,456 CITATIONS

[SEE PROFILE](#)



[Sergei O. Kucheyev](#)

Lawrence Livermore National Laboratory

200 PUBLICATIONS 4,112 CITATIONS

[SEE PROFILE](#)



[Tammy Y. Olson](#)

Lawrence Livermore National Laboratory

18 PUBLICATIONS 1,026 CITATIONS

[SEE PROFILE](#)



[Alex Hamza](#)

Lawrence Livermore National Laboratory

299 PUBLICATIONS 6,888 CITATIONS

[SEE PROFILE](#)

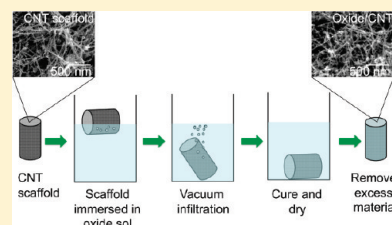
Carbon Scaffolds for Stiff and Highly Conductive Monolithic Oxide–Carbon Nanotube Composites

Marcus A. Worsley,* Sergei O. Kucheyev, Joshua D. Kuntz, Tammy Y. Olson, T. Yong-Jin Han, Alex V. Hamza, Joe H. Satcher, Jr., and Theodore F. Baumann

Physical and Life Sciences Directorate, Lawrence Livermore National Laboratory, 7000 East Avenue, Livermore, California 94550, United States

ABSTRACT: The ultra low density, high electrical conductivity, and mechanical robustness of carbon nanotube aerogels (SWNT-CA) make them ideal scaffolds around which to create novel composites. Here we report on the synthesis and characterization of oxide/carbon nanotube composites fabricated through the sol–gel deposition of oxide coatings (SiO_2 , SnO_2 or TiO_2) on SWNT-CA. The porous network of the SWNT-CA scaffold is retained after the deposition and drying process. In each case, the deposited oxide appears to form a uniform coating on the surfaces of aerogel ligaments. The composite materials exhibit high electrical conductivity (~ 100 S/m) and enhanced mechanical properties relative to the uncoated SWNT-CA support. In addition, the oxide/SWNT-CA composites possess high surface areas (as high as 742 m^2/g) and large mesopore volumes (as high as 2.2 cm^3/g). This approach offers viability in engineering new oxide/CNT composites for applications such as energy storage, sensing, and catalysis.

KEYWORDS:



INTRODUCTION

Nanocomposites of carbon nanotubes (CNTs) and various oxides¹ are among the most researched functional materials because of their many extraordinary properties in electronic,^{2–8} storage,^{9–13} structural,^{14–17} catalytic,^{18–23} and sensing^{24–27} applications. The range of composites fabricated covers many oxides, and the methods for combining the oxides and CNTs include mechanical mixing, sol–gel coating, chemical and physical vapor deposition, hydrothermal methods, and more.¹ Although much of the existing research involves the use of loose CNT powder or vertical CNT arrays in the preparation of the nanocomposite, a number of technologies would benefit from the design of composites from free-standing three-dimensional (3D) monoliths of interconnected CNTs.^{4,5,9,19} For example, in battery applications composite powders or arrays typically require addition of significant amounts of nonactive material (binder, metal conductor, or a metal substrate to support the array) to create a working electrode. Alternatively, integration of the active material into a mechanically robust and electrically conductive 3D CNT scaffold structure would eliminate the need for the nonactive material, greatly increasing the energy density of the system. Furthermore, if the 3D CNT assembly were both scalable and possessed isotropic mechanical stability, in contrast to vertical CNT arrays which are limited to millimeters in height and possess anisotropic properties, it would be amenable to a greater number of different deposition methods (solution- or gas-phase) and significantly improve versatility in the design and manufacturing for many applications.

We recently reported on a new class of ultra low-density single-wall CNT-based carbon aerogels (SWNT-CA) that are comprised of randomly oriented CNTs cross-linked by sol–gel

derived graphitic carbon nanoparticles.²⁸ These materials exhibit high electrical conductivity and robust mechanical properties at densities as low as 10 mg/cm^3 without additional reinforcement. In addition, the SWNT-CAs are structurally stable across temperatures ranging from a few Kelvin to over 1700 K (inert atmosphere) and can be fabricated as conformable monoliths with macroscopic dimensions. Therefore, these materials serve as attractive platforms for the fabrication of new monolithic CNT composite structures. We previously demonstrated the utility of these SWNT-CAs as scaffolds in the preparation of nonporous polymer/SWNT-CA composites with extraordinary electrical conductivity and mechanical properties.²⁹ In these composite structures, the free pore volume of the SWNT-CA is completely filled with polymer through direct infiltration of the monolithic support. These materials, with as little as 1 vol% of the SWNT-CA support, exhibited a 3-fold improvement in elastic modulus compared to the polymer alone. The electrical conductivity of the composite was also high (100 S/m), indicating that the network structure of the SWNT-CA was sufficiently robust to handle infiltration and curing of the polymer. Extension of this approach to other classes of materials, such as oxide/CNT composites, would provide strong evidence for the potential of the 3D SWNT-CA scaffold in the design of new nanocomposite structures.

In the work presented here, we describe the fabrication of novel oxide/SWNT-CA composites through the sol–gel deposition of oxides on the surface of nanoligaments of SWNT-CA monoliths. Unlike the nonporous polymer/SWNT-CA

Received: February 9, 2011

Revised: April 13, 2011

composites, the oxide is deposited as a conformal overlayer on the primary ligament structure of the SWNT-CA support, thus preserving open porosity within the monolithic part. This work specifically focuses on nanoporous composites prepared with SiO_2 , SnO_2 and TiO_2 coatings due to the technological interest in each of these materials. In particular, composites of SiO_2 and CNTs^{30–33} possess desirable properties for a wide range of applications such as electrochemical devices,³⁴ catalysis,³⁵ sensors,²⁵ optoelectronics⁸ and separations.³⁶ SnO_2 /CNT composites³⁷ have shown potential as sensors,^{24,26} catalyst supports,^{18,21} and Li-ion battery electrodes,^{10,13,23,38–41} whereas TiO_2 /CNT composites^{6,31,32,42} are of interest because of their potential impact in fields of catalysis,^{23,43–45} photoelectronics,⁵ and energy storage.^{11,46} Structural characterization of the oxide/SWNT-CA composites shows that, in each case, sol–gel deposition of the oxide coating occurs primarily on the surfaces of CNT ligaments throughout the aerogel monolith. In addition, these composite structures retain the high electrical conductivity of the SWNT-CA support and exhibit significant enhancements in mechanical properties relative to the uncoated aerogel structure. The approach described here provides a straightforward route to the design of porous and monolithic oxide/CNT composites for use in a variety of applications.

■ EXPERIMENTAL SECTION

Oxide/SWNT-CA Composite Preparation. The SWNT-CA nanoporous supports, with a SWNT loading of 55 wt % of solids (1 vol%) and a monolith density of 30 mg/cm³, were prepared as previously described.²⁸ The oxide/SWNT-CA composites were prepared through deposition of an oxide coating over the inner surface area of the SWNT-CA framework using sol–gel chemistry. The oxide sol–gel solutions were also synthesized using literature methods.^{47–49} The SiO_2 sol–gel was prepared via traditional one-step base-catalyzed alkoxide sol–gel chemistry using tetramethoxysilane (4.1 g), water (1.5 g), ammonium hydroxide (30%, 200 μL), and methanol (24 g).⁴⁹ The TiO_2 sol–gel was prepared via a two-step process involving acid-catalyzed hydrolysis of titanium(IV) ethoxide (1 g) using water (85.7 μL), hydrochloric acid (37%, 71.4 μL), and ethanol (3.57 g), followed by base-initiated gelation using propylene oxide (0.357 g).⁴⁷ The SnO_2 sol–gel was prepared via an epoxide-initiated gelation method using tin chloride pentahydrate (0.56 g), trimethylene oxide (1.03 g), ethanol (7 g), and water (5 g).⁴⁸ Composites were synthesized by infiltration of SWNT-CA monoliths by the oxide sol–gel solutions prior to gelation. The SWNT-CA's were immersed in the sol–gel solutions and placed under vacuum until no more air escaped from the scaffolds, indicating full penetration of the sol. The concentration of inorganic precursors was kept low to promote the growth of the condensed inorganic phase primarily on the surfaces of the SWNT-CA framework, while minimizing gelation in the free pore volume of the aerogel. The infiltrated SWNT-CAs were then cured at room temperature for 72 h to produce the wet oxide/SWNT-CA gels. The wet oxide/SWNT-CA gels were dried using supercritical extraction with liquid CO_2 to yield the final dry oxide/SWNT-CA composites.

Characterization. Bulk densities of the samples were determined from the physical dimensions and mass of each sample. The volume percent of CNT in each sample was calculated from the initial mass of SWNTs added, with an assumption of a CNT density⁵⁰ of 1.6 g/cm³, and the final volume of the aerogel. Scanning electron microscopy (SEM) characterization was performed on a JEOL 7401-F at 5–10 keV in secondary electron imaging mode with a working distance of 2–8 mm. Due to good electrical conductivity of the CNT scaffold, no conductive coating of specimens was required before SEM imaging.

Transmission electron microscopy (TEM) characterization was performed on a Phillips CM-300FEG electron microscope operated at 300 kV. Samples for TEM were prepared by pulverizing aerogels above TEM grids. Surface area determination and pore volume and size analysis were performed by Brunauer–Emmett–Teller (BET) and Barrett–Joyner–Halenda (BJH) methods using an ASAP 2010 Surface Area Analyzer (Micromeritics Instrument Corporation).⁵¹ Samples of approximately 0.1 g were heated to 150 °C under vacuum (10^{-5} Torr) for at least 24 h to remove adsorbed species prior to analysis. Ultraviolet–visible (UV–vis) absorption spectroscopy was performed on a Perkin-Elmer Lambda 950. Samples for UV–vis analysis were prepared by suspension of pulverized material in ethanol via ultrasonication. The titania contribution curve was generated by subtracting the raw SWNT-CA spectrum from the raw TiO_2 /SWNT-CA spectrum. No scaling was necessary as the background signals from both aerogels were of the same intensity.

Powder X-ray diffraction (XRD) analysis of the samples was performed with $\text{Cu K}\alpha$ radiation on a Scintag PAD-V X-ray diffractometer. Rutile TiO_2 powder was used as a standard. Oxide content was determined using thermogravimetric analysis (TGA) performed on a Shimadzu TGA 50 Thermogravimetric Analyzer. Samples were heated in air to 1000 °C at 10 °C/min in alumina boats. The residual mass was considered the oxide content. Electrical conductivity was measured using the four-probe method with metal electrodes attached to the ends of cylindrical samples. The amount of current transmitted through the sample during measurement was 100 mA, and the voltage drop along the sample was measured over distances of 3–6 mm. Seven or more measurements were taken on each sample, and results were averaged.

Mechanical properties were studied by indentation in an MTS XP Nanoindenter with a spherical sapphire indenter with a radius of 496 μm . Before indentation, aerogel monoliths were attached to silicon wafers with epoxy. A series of both continuous and partial load-unload indents (with an unloading percentage of 100%) was carried out under ambient conditions. The loading rate was continuously adjusted to keep a constant representative strain rate of $1 \times 10^{-3} \text{ s}^{-1}$, as discussed previously.⁵² Young's modulus was calculated according to the method of Oliver and Pharr.⁵³ We assume Poisson's ratios of sapphire and aerogels of 0.23 and 0.20, respectively, and the Young's modulus of sapphire of 425 GPa.⁵² For each specimen, from 8 to 12 measurements were taken from different locations, and results were averaged. Error bars given in the tables for the Young's modulus are the standard error in the mean.

■ RESULTS AND DISCUSSION

Examination of the composite structures by SEM (Figures 1–2) shows that the porous network structure of the SWNT-CA support is maintained after the oxide deposition and drying process. Additionally, in each case, the deposited oxide appears to form a uniform coating on the surfaces of the CNT ligaments. For example, the SEM images for the SiO_2 /SWNT-CA composite show that the deposited SiO_2 aerogel particles preferentially coat the CNT bundles, as very few unsupported SiO_2 particles were observed (Figure 1a,b). Similarly, the SEM images for the SnO_2 /SWNT-CA show that the majority of SnO_2 particles are associated with the CNT network (Figure 2). Unlike the SiO_2 composite, however, the deposited SnO_2 particles are crystalline with diameters of ~ 3 –5 nm, consistent with previous reports for SnO_2 aerogels prepared using a similar sol–gel formulation.⁴⁸ The TiO_2 particles, as deposited, are amorphous but can be converted to the anatase phase after calcination at 320 °C for 5 h in air, as indicated by XRD (Figure 3). After annealing, the TiO_2 nanocrystals are easily distinguishable by both SEM and TEM

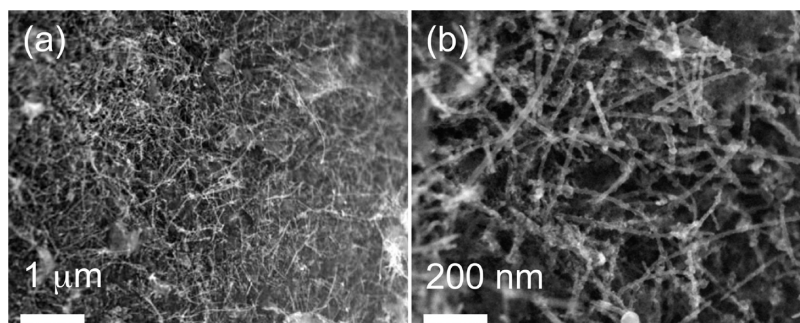


Figure 1. SEM images of SiO₂/SWNT-CA composites at (a) low and (b) high magnifications.

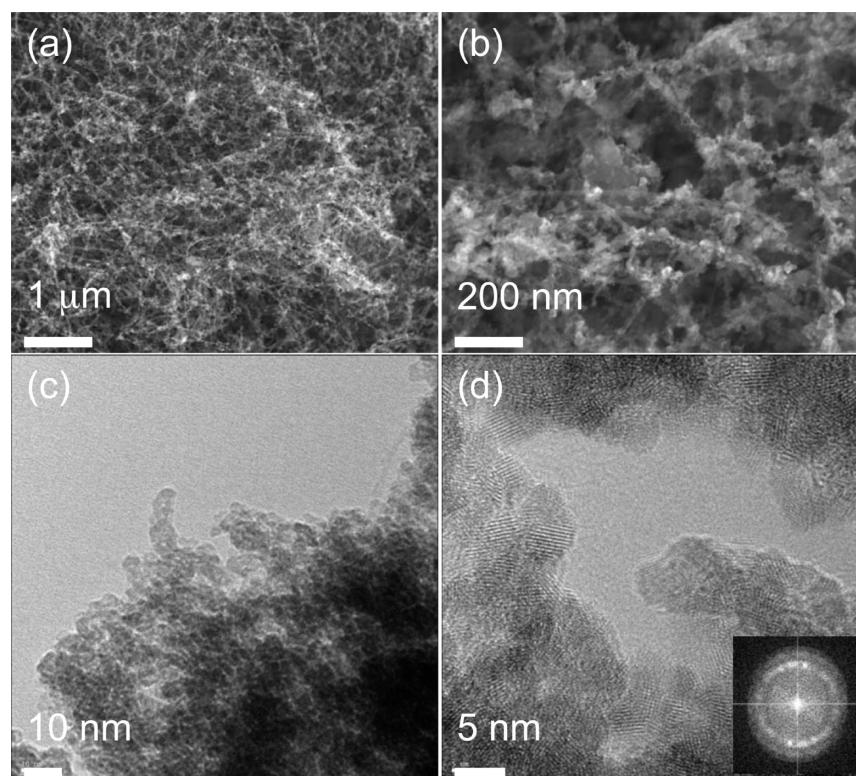


Figure 2. SEM images of SnO₂/SWNT-CA composites at (a) low and (b) high magnifications. TEM images of SnO₂/SWNT-CA composites at (c) low and (d) high magnification. Inset in (d) is the electron diffraction pattern of the SnO₂/SWNT-CA.

from the underlying support structure (Figure 4). The electron diffraction pattern (the inset in Figure 4f) further confirms the crystalline nature of the TiO₂ particles after annealing.

Not surprisingly, the gas adsorption properties of the oxide/SWNT-CA composites are quite different from those of the uncoated support material. As shown in Figures 5–7, the nitrogen isotherms for these composite structures are consistent with materials comprised of both meso- and macropores. Because the SWNT-CA support is primarily a macroporous structure, the mesoporosity in these materials can be attributed to the porous oxide coating. Each of the composite structures exhibits larger surface area and mesopore volume than those respective values for the SWNT-CA support, which are similar to surface areas observed in pure metal oxide aerogels.^{47–49,54,55} Notably, the BET surface area (742 m²/g) and mesopore volume (2.2 cm³/g) measured for the SiO₂/SWNT-CA composite are

considerably larger than the values measured for the SWNT-CA support (162 m²/g, 0.3 cm³/g) and on par with values observed in the pure SiO₂ aerogel (670 m²/g, 1.8 cm³/g). This change in textural properties has been observed with other SiO₂/CNT composites.³⁶ The SnO₂ composite also exhibits significant increases in BET surface area (349 m²/g) and mesopore volume (0.9 cm³/g) relative to the support structure. Interestingly, the crystalline TiO₂/SWNT-CA composite has a greater mesopore volume than the amorphous composite (1.1 vs 0.6 cm³/g), whereas the BET surface areas remain similar (197 and 202 m²/g for crystalline and amorphous composites, respectively). Thus, crystallization of the deposited TiO₂ particles was achieved without loss of accessible surface area. The high surface areas and large mesopore volumes associated with these composite materials would be expected to be beneficial for energy storage, catalyst, and sensing applications.

Structural integrity and electrical conductivity are also important considerations in designing porous structures for use as

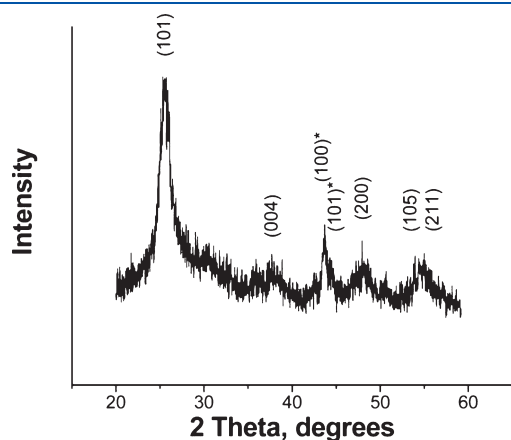


Figure 3. Powder X-ray diffraction spectrum for a TiO_2 /SWNT-CA composite annealed at 320 °C. Asterisks indicate peaks indexed to graphite. All other peaks indexed to anatase phase TiO_2 .

catalyst supports and electrodes. Therefore, the mechanical and electrical properties of the composite structures were evaluated (Tables 1 and 2 and Figure 8). The electrical conductivities of each of the oxide-coated composites are similar to that of the uncoated SWNT-CA structure, suggesting that the conductive CNT network is intact after deposition and supercritical drying. This observation is consistent with our previous results for polymer/SWNT-CA composites.²⁹

Mechanical properties of the composites show a more complex behavior than that of electrical conductivity. For example, Figure 8 compares continuous load–displacement curves for a SiO_2 /SWNT-CA composite, a SiO_2 aerogel, and a SWNT-CA scaffold. It is seen from Figure 8 that, for the maximum load used, the deformation of the SWNT-CA scaffold is purely elastic with a modulus of 1.2 MPa (Table 1). This is consistent with our previous report.²⁸ In contrast, the deformation of the silica aerogel has a large inelastic component, which is evidenced by a difference in loading and unloading curves and a large residual displacement of $\sim 30\mu\text{m}$. This behavior is in contrast to an almost entirely elastic deformation of TMOS-derived base-catalyzed SiO_2 aerogels prepared slightly differently and reported previously.⁵² All three oxide aerogels studied in the present work (silica, titania, and

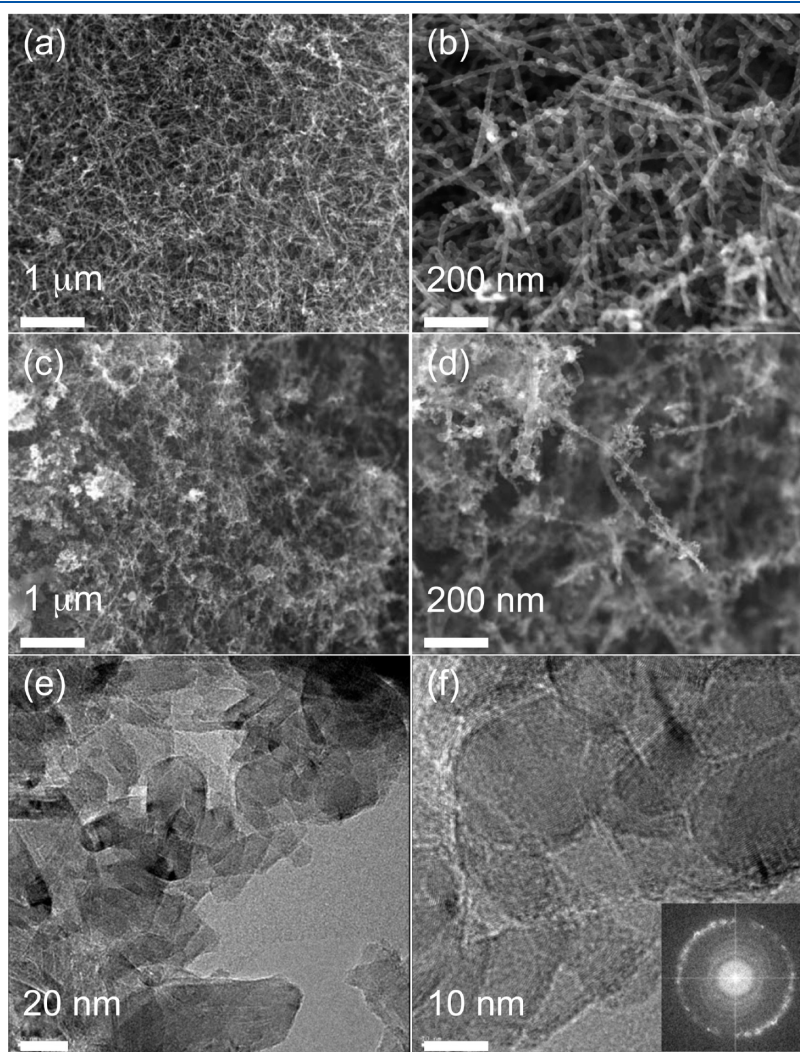


Figure 4. SEM images of (a, b) as-synthesized and (c, d) annealed at 320 °C TiO_2 /SWNT-CA composites at low and high magnifications. TEM images of annealed (e, f) TiO_2 /SWNT-CA composites at low and high magnifications. Inset in (f) is the electron diffraction pattern of the annealed TiO_2 /SWNT-CA.

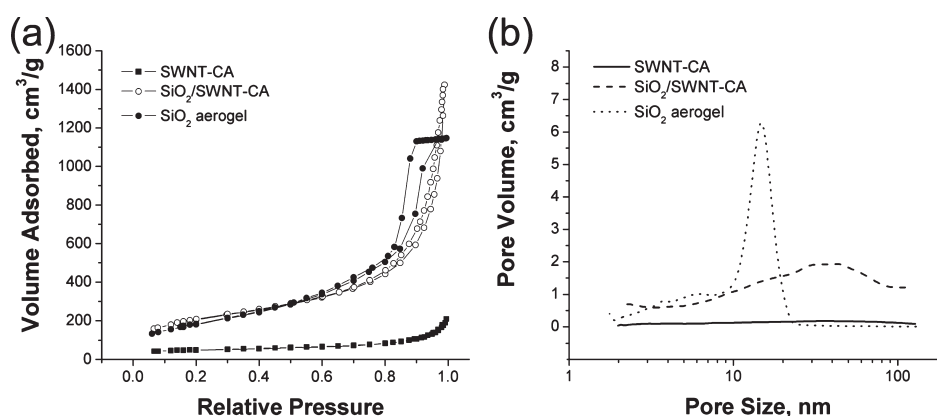


Figure 5. Plots of the (a) nitrogen adsorption/desorption isotherms and (b) pore size distribution for SiO₂/SWNT-CA, SWNT-CA, and bulk SiO₂.

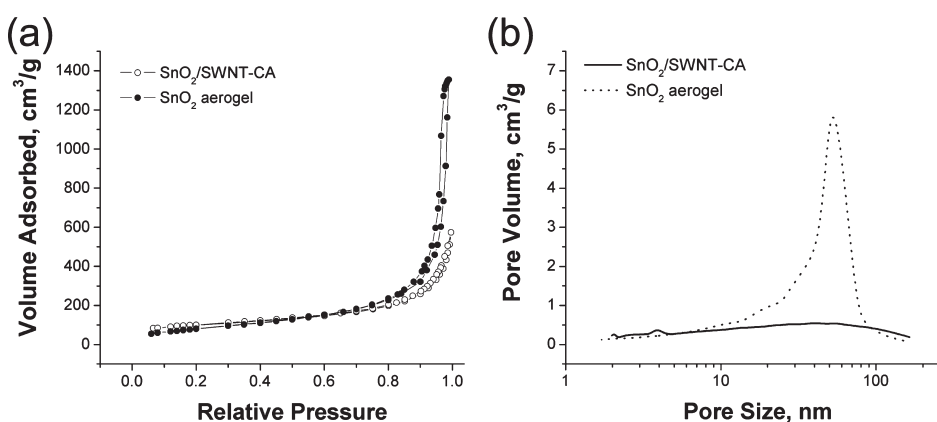


Figure 6. Plots of the (a) nitrogen adsorption/desorption isotherms and (b) pore size distribution for SnO₂/SWNT-CA and bulk SnO₂.

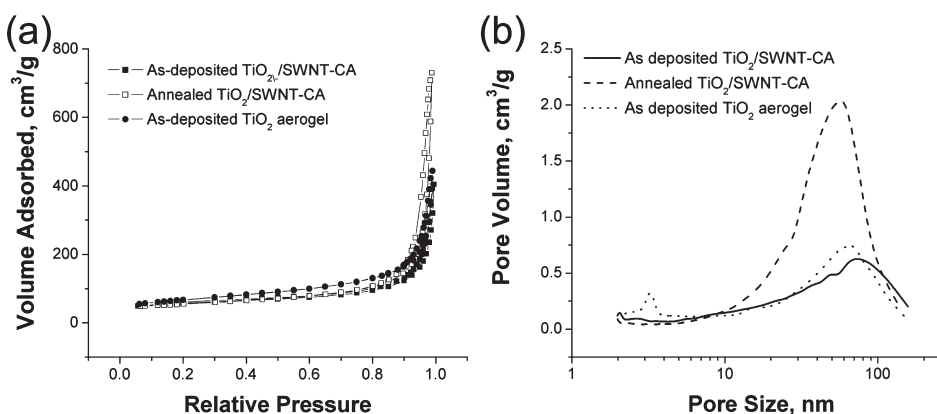


Figure 7. Plots of the (a) nitrogen adsorption/desorption isotherms and (b) pore size distribution for TiO₂/SWNT-CA (as-deposited and annealed) and bulk TiO₂.

stannic oxide) exhibit a relatively large inelastic response for maximum effective strains similar to those of Figure 8. The oxide/SWNT-CA composites of SiO₂ and TiO₂ also behave inelastically (Figure 8), whereas SnO₂/SWNT-CA composites retained very elastic properties of the CNT-based scaffold.

Although elastic properties of aerogels can be, at least qualitatively, related to structure connectivity (i.e., to how the nanoligaments are interconnected into a three-dimensional structure),

the mechanisms of inelastic deformation of aerogels are not understood. Neither is it clear which steps of aerogel preparation have a dominant effect on inelastic properties, and more work is currently needed to understand inelastic deformation of aerogels. Hence, we turn to a more detailed analysis of Young's modulus (E) data.

In any analysis of the mechanical deformation behavior of porous solids, the first parameter to consider is the monolith

Table 1. Physical Properties of SWNT-CA Scaffold, Bulk SiO₂, SiO₂/SWNT-CA, Bulk SnO₂, and SnO₂/SWNT-CA Composite

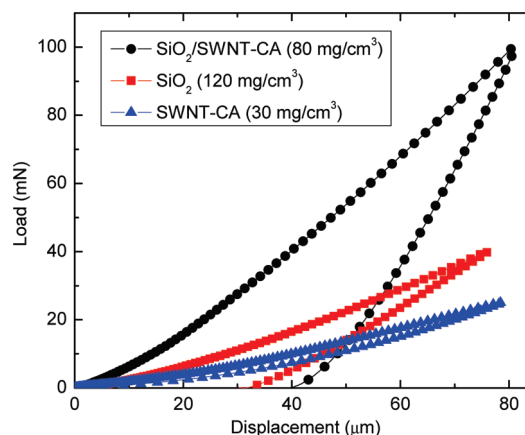
material	CNT (vol %) (wt %)	density (g/cm ³)	<i>E</i> (MPa)	σ (S cm ⁻¹)
SWNT-CA	1 (55)	0.028	1.2 ± 0.1	1.12
SiO ₂	0	0.120	2.4 ± 0.2	<0.001
SiO ₂ /SWNT-CA	1 (16)	0.080	7.3 ± 0.4	1.00
SnO ₂	0	0.204	3.6 ± 1.7	<0.001
SnO ₂ /SWNT-CA	1 (33)	0.046	1.0 ± 0.2	1.00

Table 2. Physical Properties of Bulk TiO₂ and TiO₂/SWNT-CA Composites (amorphous and crystalline)

material	CNT (vol %) (wt%)	density (g/cm ³)	<i>E</i> (MPa)
TiO ₂	0	0.193	3.5 ± 0.2
TiO ₂ /SWNT-CA (amorphous)	1 (16)	0.082	17.3 ± 1.7
TiO ₂ /SWNT-CA (crystalline)	2 (23)	0.108	14.9 ± 0.7

density because mechanical properties depend superlinearly on the density.²⁸ Because of differences in the geometry and connectivity of ligaments, different aerogels exhibit different scaling behavior of *E* on the monolith density (ρ). In particular, for TMOS-derived base-catalyzed SiO₂ aerogels, as studied in this work, the *E* scales as $E \sim \rho^{3.7}$,⁵⁶ whereas for our CNT-based and conventional carbon aerogels, $E \sim \rho^{2.7}$.²⁸ The SiO₂/SWNT-CA composite aerogel with a monolith density of 80 mg/cm³ is made of 30 mg/cm³ of carbon and 50 mg/cm³ of SiO₂. The analysis for SiO₂/CNT composites is further simplified by the fact that the mass densities of ligaments in both aerogels are similar (~ 2 g/cm³). If such a composite aerogel were made from two interpenetrating and not cross-linked networks of carbon and SiO₂ nanoligaments with monolith densities of 30 and 50 mg/cm³, the contribution to the elastic modulus from carbon and SiO₂ networks would be ~ 1 and 0.1 MPa, respectively.^{28,56} Hence, a much larger Young's modulus of ~ 7 MPa of the SiO₂/SWNT-CA composite (Table 1) is consistent with electron microscopy observations (Figure 1) that the composite aerogel has morphology of the carbon scaffold with SiO₂ particles decorating carbon ligaments rather than of two interpenetrating but poorly cross-linked SiO₂ and carbon networks.

This scaling law analysis could be extended further by noting that a CNT-based aerogel with a density of 80 mg/cm³ has a Young's modulus of ~ 15 MPa,²⁸ which is close to the modulus of the SiO₂/CNT composite (~ 7 MPa). A factor of 2 lower modulus of the composite could be attributed to significantly weaker atomic bonds in SiO₂ (and, hence, a lower *E*) as compared to the case of graphitic carbon. Indeed, the Young's modulus of full density amorphous silica is ~ 70 GPa as compared to typical ~ 200 – 400 GPa modulus values for graphitic carbon fibers. Hence, coating of carbon aerogel ligaments with SiO₂ nanoparticles has a mechanical reinforcement effect comparable to that of increasing the density of the carbon scaffold, suggesting good adhesion between the deposited SiO₂ nanoparticles and the SWNT-CA support.

**Figure 8.** Continuous load–displacement curves for the SiO₂/SWNT-CA composite, SiO₂ aerogel, and SWNT-CA scaffold. Monolith densities are given in the legend.

An even greater increase in the elastic modulus is observed in TiO₂/SWNT-CA composites, for both amorphous and crystalline (anatase) TiO₂/SWNT-CA composites (Tables 1 and 2). Because the weight density of full-density TiO₂ is about twice that of graphitic carbon and Young's moduli of full-density TiO₂ and graphitic carbon are similar, a uniform coating of a SWNT-CA scaffold with an initial density of 30 mg/cm³ with TiO₂ with a volumetric weight density of 50 mg/cm³ is comparable to a case of a purely carbon nanofoam with a monolithic density of $\sim 30 + 50 \cdot 2/4 = 55$ mg/cm³. According to the *E* scaling behavior for CNT-aerogels,²⁸ such a carbon aerogel has $E \sim 6$ MPa, which is three times lower than *E* for the TiO₂/SWNT-CA composite (Table 2). This could be attributed to additional cross-linking of ligaments by TiO₂ particles as opposed to a less efficient process of a uniform coating of ligaments of the carbon scaffold. The cross-linking effectively changes the connectivity of the ligament network and improves mechanical properties and their scaling behavior.

Table 1 shows that, in contrast to the cases for SiO₂ and TiO₂, mechanical properties of the SnO₂/SWNT-CA composite are dominated by those of the CNT scaffold. This difference in reinforcement may be related to different amounts of oxide deposited on the SWNT-CA (33 wt % for SnO₂ vs 70 wt % for SiO₂ and TiO₂), resulting in an increase of the monolith density by ~ 17 at.% for SnO₂ vs ~ 167 and ~ 83 at.% for SiO₂ and TiO₂, respectively. Alternatively, such differences could also arise from different interfacial interactions between the deposited oxide and the SWNT-CA support due to the different reaction chemistries used to deposit oxide coatings. Additional studies of deformation behavior of carbon aerogels with variable loading of SnO₂ could provide insight into the structure–property correlation of SnO₂/SWNT-CA composites.

Composites of TiO₂ and carbon have been shown to exhibit higher photocatalytic activity over a wider absorption band relative to TiO₂ alone. Therefore, we have also measured the UV–vis absorption spectrum of the annealed TiO₂/SWNT-CA composite as a suspension in ethanol. As shown in Figure 9, the spectrum for the TiO₂/SWNT-CA material shows not only the well-known TiO₂ absorption band around 260 nm but also absorption far into the visible at 500 nm when the contribution from the CNT scaffold is removed (the inset in Figure 9). This widening of the absorption band in TiO₂/C composites is

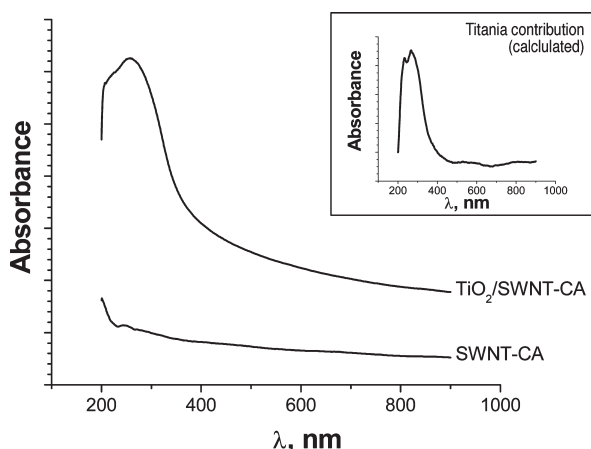


Figure 9. UV-vis absorption spectra for TiO₂/SWNT-CA and SWNT-CA. Spectra are offset for clarity. Inset shows contribution of TiO₂ nanoparticles in TiO₂/SWNT-CA (SWNT-CA spectrum subtracted).

well-documented in the literature and is another reason why TiO₂/CNT composites are of such high interest.⁵⁷

CONCLUSIONS

In summary, novel oxide/CNT nanocomposites were fabricated through the deposition of oxide coatings on monolithic SWNT-CAs supports. Infiltration and deposition of the oxides were achieved with little to no degradation of the extended CNT network of the support, yielding highly conductive nanocomposites. Significant mechanical reinforcement was also observed. In addition, the oxide/CNT nanocomposites exhibited high surface areas and large internal pore volumes. The monolithic nature of these oxide/SWNT-CA assemblies should prove advantageous for a number of applications, such as battery electrodes, sensing devices, and catalysts. These results, along with those for the polymer/SWNT-CA composites, show the versatility and potential of the 3D CNT scaffold approach.

AUTHOR INFORMATION

Corresponding Author

*E-mail: worsley1@llnl.gov.

ACKNOWLEDGMENT

This work was performed under the auspices of the U.S. Department of Energy by Lawrence Livermore National Laboratory under Contract DE-AC52-07NA27344 and funded by the DOE Office of Energy Efficiency and Renewable Energy.

REFERENCES

- (1) Eder, D. *Chem. Rev.* **2010**, *110* (3), 1348.
- (2) Giovanardi, R.; Montorsi, M.; Ori, G.; Cho, J.; Subhani, T.; Boccaccini, A. R.; Siligardi, C. *J. Mater. Chem.* **2010**, *20* (2), 308–313.
- (3) Zhou, J. G.; Fang, H. T.; Maley, J. M.; Ko, J. Y. P.; Murphy, M.; Chu, Y.; Sammynaiken, R.; Sham, T. K. *J. Phys. Chem. C* **2009**, *113* (15), 6114.
- (4) Pan, J. Y.; Zhu, C. C.; Gao, Y. L. *Appl. Surf. Sci.* **2008**, *254* (13), 3787–3792.
- (5) Yang, Y. D.; Qu, L. T.; Dai, L. M.; Kang, T. S.; Durstock, M. *Adv. Mater.* **2007**, *19* (9), 1239–+.

- (6) Yu, H. T.; Quan, X.; Chen, S.; Zhao, H. M. *J. Phys. Chem. C* **2007**, *111* (35), 12987–12991.
- (7) Chen, C. S.; Chen, X. H.; Yi, B.; Lu, T. G.; Li, W. H.; Xu, L. S.; Yang, Z.; Zhang, H.; Wang, Y. G. *Acta Materialia* **2006**, *54* (20), 5401–5407.
- (8) Olek, M.; Busgen, T.; Hilgendorff, M.; Giersig, M. *J. Phys. Chem. B* **2006**, *110* (26), 12901–12904.
- (9) Bakhoun, E. G.; Cheng, M. H. M. *J. Appl. Phys.* **2009**, *105* (10), No. 104314.
- (10) Chen, G.; Wang, Z. Y.; Xia, D. G. *Chem. Mater.* **2008**, *20* (22), 6951–6956.
- (11) Mishra, A.; Banerjee, S.; Mohapatra, S. K.; Graeve, O. A.; Misra, M. *Nanotechnology* **2008**, *19* (44), 445607.
- (12) Zhang, Y. P.; Sun, X. W.; Pan, L. K.; Li, H. B.; Sun, Z.; Sun, C. P.; Tay, B. K. *Solid State Ionics* **2009**, *180* (32–35), 1525–1528.
- (13) Du, G.; Zhong, C.; Zhang, P.; Guo, Z.; Chen, Z.; Liu, H. *Electrochim. Acta* **2010**, *55* (7), 2582.
- (14) Chu, B. T. T.; Tobias, G.; Salzmann, C. G.; Ballesteros, B.; Grobert, N.; Todd, R. I.; Green, M. L. H. *J. Mater. Chem.* **2008**, *18* (44), 5344.
- (15) Ning, J.; Zhang, J.; Pan, Y.; Guo, J. *Mater. Sci. Eng. A* **2003**, *357* (1–2), 392.
- (16) Lin Hwang, G.; Chu Hwang, K. *J. Mater. Chem.* **1991**, *1* (6), 2001.
- (17) Flahaut, E.; Peigney, A.; Laurent, C.; Marlière, C.; Chastel, F.; Roussel, A. *Acta Materialia* **2000**, *48* (14), 3803.
- (18) Hsu, R. S.; Higgins, D.; Chen, Z. *Nanotechnology* **2010**, *21* (16), 165705.
- (19) Khanderi, J.; Hoffmann, R. C.; Schneider, J. J. *Nanoscale* **2010**, *2* (4), 613–622.
- (20) Zhou, X.; Li, Y. Z.; Peng, T.; Xie, W.; Zhao, X. J. *Mater. Lett.* **2009**, *63* (20), 1747–1749.
- (21) Du, C.; Chen, M.; Cao, X.; Yin, G.; Shi, P. *Electrochem. Commun.* **2009**, *11* (2), 496.
- (22) Byrappa, K.; Dayananda, A. S.; Sajan, C. P.; Basavalingu, B.; Shayan, M. B.; Soga, K.; Yoshimura, M. *J. Mater. Sci.* **2008**, *43* (7), 2348–2355.
- (23) An, G. M.; Ma, W. H.; Sun, Z. Y.; Liu, Z. M.; Han, B. X.; Miao, S. D.; Miao, Z. J.; Ding, K. L. *Carbon* **2007**, *45* (9), 1795–1801.
- (24) Yang, M.; Kim, D.-H.; Kim, W.-S.; Kang, T. J.; Lee, B. Y.; Hong, S.; Kim, Y. H.; Hong, S.-H. *Nanotechnology* **2010**, *21* (21), 215501.
- (25) Guo, S. J.; Li, J.; Ren, W.; Wen, D.; Dong, S. J.; Wang, E. K. *Chem. Mater.* **2009**, *21* (11), 2247–2257.
- (26) Gong, J.; Sun, J.; Chen, Q. *Sens. Actuators, B* **2008**, *130* (2), 829.
- (27) Guirado-Lopez, R. A.; Sanchez, M.; Rincon, M. E. *J. Phys. Chem. C* **2007**, *111* (1), 57–65.
- (28) Worsley, M. A.; Kucheyev, S. O.; Satcher, J. H.; Hamza, A. V.; Baumann, T. F. *Appl. Phys. Lett.* **2009**, *94* (7), 073115.
- (29) Worsley, M. A.; Kucheyev, S. O.; Kuntz, J. D.; Hamza, A. V.; Satcher, J. H.; Baumann, T. F. *J. Mater. Chem.* **2009**, *19* (21), 3370.
- (30) Ding, K. L.; Hu, B. J.; Xie, Y.; An, G. M.; Tao, R. T.; Zhang, H. Y.; Liu, Z. M. *J. Mater. Chem.* **2009**, *19* (22), 3725–3731.
- (31) Shin, H. S.; Jang, Y. S.; Lee, Y.; Jung, Y.; Kim, S. B.; Choi, H. C. *Adv. Mater.* **2007**, *19* (19), 2873–+.
- (32) Hernadi, K.; Ljubovic, E.; Seo, J. W.; Forro, L. *Acta Mater.* **2003**, *51* (5), 1447–1452.
- (33) Fu, Q.; Lu, C. G.; Liu, J. *Nano Lett.* **2002**, *2* (4), 329–332.
- (34) Gavalas, V. G.; Andrews, R.; Bhattacharyya, D.; Bachas, L. G. *Nano Lett.* **2001**, *1* (12), 719.
- (35) Lee, S. A.; Hong, S. H.; Kim, D. O.; Han, T. H.; Iijima, S.; Nam, J. D. *Microporous Mesoporous Mater.* **2008**, *111* (1–3), 292–299.
- (36) Zhang, M.; Wu, Y. P.; Feng, X. Z.; He, X. W.; Chen, L. X.; Zhang, Y. K. *J. Mater. Chem.* **2010**, *20* (28), 5835–5842.
- (37) Han, W.-Q.; Zettl, A. *Nano Lett.* **2003**, *3* (5), 681.
- (38) Zhu, C.-L.; Zhang, M.-L.; Qiao, Y.-J.; Gao, P.; Chen, Y.-J. *Mater. Res. Bull.* **2010**, *45* (4), 437.
- (39) Fu, Y.; Ma, R.; Shu, Y.; Cao, Z.; Ma, X. *Mater. Lett.* **1996**, *63* (22), 2009.

- (40) Chen, Y.-J.; Zhu, C.-L.; Xue, X.-Y.; Shi, X.-L.; Cao, M.-S. *Appl. Phys. Lett.* **2008**, 92 (22), 223101.
- (41) Xie, J.; Varadan, V. K. *Mater. Chem. Phys.* **2005**, 91 (2–3), 274.
- (42) Liu, B.; Zeng, H. C. *Chem. Mater.* **2008**, 20 (8), 2711–2718.
- (43) Wang, W. D.; Serp, P.; Kalck, P.; Silva, C. G.; Faria, J. L. *Mater. Res. Bull.* **2008**, 43 (4), 958–967.
- (44) Orlanducci, S.; Sessa, V.; Terranova, M. L.; Battiston, G. A.; Battiston, S.; Gerbasi, R. *Carbon* **2006**, 44 (13), 2839–2843.
- (45) Wang, W. D.; Serp, P.; Kalck, P.; Faria, J. L. *J. Mol. Catal. A: Chem.* **2005**, 235 (1–2), 194–199.
- (46) Wang, D.-W.; Fang, H.-T.; Li, F.; Chen, Z.-G.; Zhong, Q.-S.; Lu, G. Q.; Cheng, H.-M. *Adv. Funct. Mater.* **2008**, 18 (23), 3787–3793.
- (47) Kucheyev, S. O.; Baumann, T. F.; Wang, Y. M.; van Buuren, T.; Satcher, J. H. *J. Electron Spectrosc. Relat. Phenom.* **2005**, 144, 609–612.
- (48) Baumann, T. F.; Kucheyev, S. O.; Gash, A. E.; Satcher, J. H. *Adv. Mater.* **2005**, 17 (12), 1546–1548.
- (49) Iler, R. K.; *The Chemistry of Silica*; John Wiley & Sons: New York, 1979.
- (50) Bekyarova, E.; Itkis, M. E.; Cabrera, N.; Zhao, B.; Yu, A. P.; Gao, J. B.; Haddon, R. C. *J. Am. Chem. Soc.* **2005**, 127 (16), 5990–5995.
- (51) Gregg, S. J.; Sing, K. S. W., *Adsorption, Surface Area and Porosity*, 2nd ed.; Academic: London, 1982).
- (52) Kucheyev, S. O.; Hamza, A. V.; Satcher, J. H.; Worsley, M. A. *Acta Mater.* **2009**, 57 (12), 3472–3480.
- (53) Oliver, W. C.; Pharr, G. M. *J. Mater. Res.* **1992**, 7 (6), 1564–1583.
- (54) Pajonk, G. M. *Catal. Today* **1997**, 35 (3), 319–337.
- (55) Taguchi, A.; Schuth, F. *Microporous Mesoporous Mater.* **2005**, 77 (1), 1–45.
- (56) Woignier, T.; Reynes, J.; Alaoui, A. H.; Beurroies, I.; Phalippou, J. J. *Non-Cryst. Solids* **1998**, 241 (1), 45–52.
- (57) Sakthivel, S.; Kisch, H. *Angew. Chem., Int. Ed.* **2003**, 42 (40), 4908–4911.